A Piezo-Sensor-Based "Smart Tire" System for Mobile Robots and Vehicles

Jingang Yi, *Senior Member, IEEE*

***Abstract*—In this paper, we present the development of a tire rubber deformation sensing system that provides the critical information for understanding and estimation of wheel/ground interactions for mobile robots and vehicles. Polyvinylidene fluoride (PVDF)-based sensors are designed and fabricated to embed on the inner tread surface to measure the tire rubber tread deformation. Analytical models of the PVDF-based sensing system are presented to capture the wheel/ground contact information and friction characteristics. The sensed deformation measurements are integrated with the onboard control system through a wireless data transmission module. Experimental results on a skid-steered mobile robot are presented to show the feasibility and estimation of wheel/ground friction characteristics using the developed sensing system.**

***Index Terms*—Deformation, friction estimation, mobile robot, polyvinylidene fluoride (PVDF), tire/road friction.**

I. Introduction

PNEUMATIC tires are critical components in mobile systems that are widely used in our lives for passenger and goods transportation. Fundamental understanding of wheel/ground interactions is a challenging task because of high nonlinearity in wheel/ground interactions and lack of *in situ* sensing mechanisms. The recently developed tire pressure monitoring system (TPMS) cannot be used for real-time applications due to limited information. Tread deformation is one of the most critical data for understanding the wheel/ground interactions [1]–[3].

The "Darmstadt tire sensor" has been presented in [1] and [4] to measure the tire tread deformation. Surface acoustic wave (SAW) sensors are proposed for a "smart tire" application in [5]. Strain and capacitance sensors are developed in [6] and [7] for monitoring the tire tread deformation. Accelerometers have been placed inside tires for friction force estimations [8]. Optical sensors are also developed for measuring tire deformation [9]. The use of polyvinylidene fluoride (PVDF)-based sensors to measure the tread deformation is presented in [10]. All of the aforementioned work of "smart tire" sensors, however, do not provide a systematic estimation scheme for quantitatively predicting wheel/ground friction characteristics. In this paper, we discuss and extend a PVDF-based "smart tire" sensing system in [10] for mobile robots and vehicles. Polymer-based PVDF sensors have the distinctive advantages of low cost, high flexibility, and strong compatibility with wheel tread materials (e.g., rubber) in comparison with other types of piezo-sensors, such as silicon- and ceramics-based sensors.

A skid-steered mobile robot is chosen as the testing platform in this study because of its simple mechanism and robustness. For skid-steered robots, steering mechanism is achieved through differential wheel speeds. Methods of modeling tracked ground vehicles have been utilized for skid-steered mobile robots. An extra wheeled trailer is designed in [11] to experimentally study the kinematic relationship for a skid-steered robot, and it is concluded that a kinematic model for an ideal differential-driven wheeled robot (e.g., unicycle-like robot) cannot be used for skid-steered robots. A kinematic and dynamic model is presented in [12] and a slip-based adaptive tracking control system is designed for skid-steered robots. A low-cost inertial measurement unit (IMU)-based simultaneous localization and slip estimation scheme is proposed in [13] to integrate velocity constraints and estimates into a nonlinear Kalman filter (KF) without the need of GPS information. In this study, we use the slip estimation and robot localization scheme in [13] to provide kinematic information of the robot motion.

We report the development of the "smart tire" mechatronic system for skid-steered mobile robots. We focus on how to obtain the wheel/ground interaction information from the integrated "smart tire" sensing system with other onboard intelligent devices. An analytical model for the PVDF-based tread deformation sensors is first presented. The goal of the sensor model is to provide a relationship between sensor measurements and the information of wheel/ground interactions, such as wheel slip, friction coefficient, etc. We then describe a prototype of the sensing system and demonstrate experimental results. The contribution of this study is twofold. First, we discuss a new sensing method to capture the *in situ* wheel/ground interaction information. We also provide an analytical model to interpret the sensed measurement. Second, the integration of the developed "smart tire" sensing system with other onboard devices and algorithms provides a new mechanism to study complex dynamic interactions between deformable and rigid bodies, such as tire and ground.

The remainder of this paper is organized as follows. We discuss briefly the skid-steered mobile robotic platform and wheel slip estimation scheme in Section II. In Section III, we present the modeling of the PVDF-based bending sensor. Experimental results are presented in Section IV before we conclude the paper in Section V.

Manuscript received August 31, 2007; revised December 12, 2007. Recommended by Guest Editors F. Karray and C. W. de Silva. This work was supported in part by the Texas Transportation Institute (TTI). This paper was presented in part at the 2007 SPIE Conference on Sensors and Smart Structures Technologies for Civil, Mechanical, and Aerospace Systems, San Diego, CA, March 19–22, 2007.

The author is with the Department of Mechanical Engineering, San Diego State University, San Diego, CA 92182 USA (e-mail: jgyi@mail.sdsu.edu.)

Color versions of one or more of the figures in this paper are available online at http://ieeexplore.ieee.org.

Digital Object Identifier 10.1109/TMECH.2007.915064

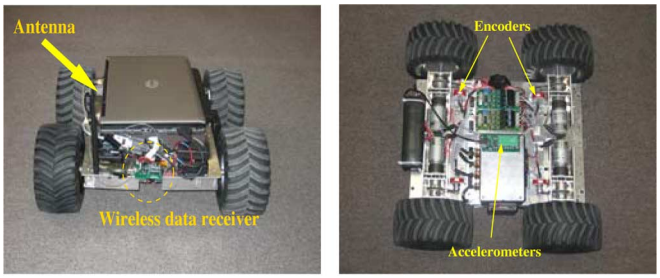

(a) (b)

Fig. 1. Skid-steered four-wheel mobile robot with a sensor suite.

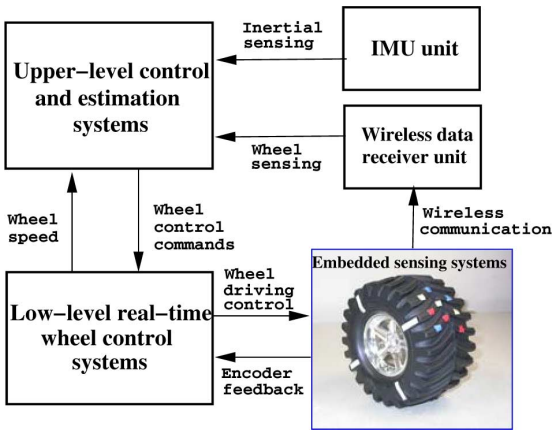

Fig. 2. Flowchart for the sensing and control systems of the skid-steered mobile robot.

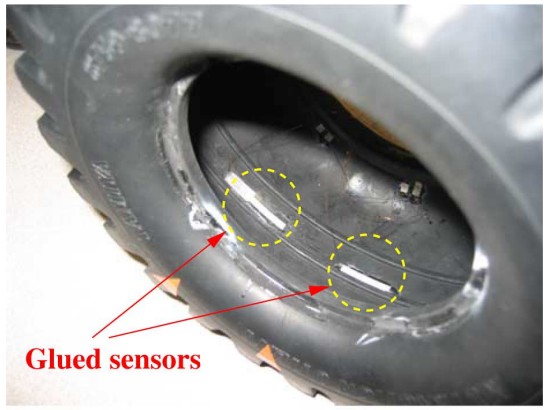

(a)

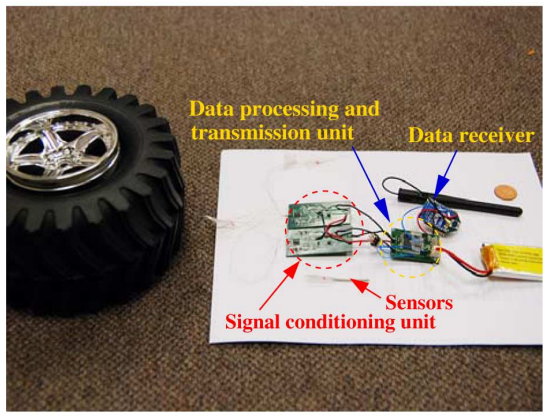

(b)

Fig. 3. (a) Two glued deformation sensors inside one wheel. (b) Sensor signal conditioning, processing, and wireless data transmission modules.

II. Robotic and Wheel Sensing Systems

A. Robotic Platform

The skid-steered mobile robot shown in Fig. 1 is used as a test vehicle for the wheel deformation sensing system. The sensing and control architecture of the robotic system is shown in Fig. 2. We use a low-cost IMU from Sentera Technology, Inc., to provide three-axis attitude and acceleration measurements. The four-wheel motion control is implemented on a real-time system from Acroname Robotic, Inc., with an optical wheel encoder feedback. The control system is a two-level hierarchy: the localization and slip estimation and trajectory control algorithms are located in the upper layer (onboard laptop computer system), and the PID-based motor control is located at the low-level real-time systems.

Two tire deformation sensors are attached on the inner surface of the rubber tire [see Fig. 3(a)]. The size of the PVDF sensor is 20 mm $\times$ 3 mm $\times$ 110 μm, and the PVDF film is from Measurement Specialties, Inc. Platinum is deposited on the top and bottom surfaces of the PVDF film as electrodes. The connection wire is glued on the tip of the sensor film using conductive glue. The distance between the two PVDF sensors shown in Fig. 3(a) is 30 mm.

The sensor signal conditioning, processing, and wireless data transmission units are shown in Fig. 3(b). Under tire deformation, the PVDF sensor generates a small amount of electric charge and the charge signals are converted and amplified into large voltage signals (e.g., 0–5 V). The sensor measurement is fed into a low-noise analog filter before it is sampled, A/D converted, and wireless transmitted. All electronic units are custom designed and can be fit into rotating wheels. A small battery is used to power the circuits and also located inside the wheel [see Fig. 3(b)]. A receiving unit (with an antenna) is connected to the onboard laptop. We use ZigBee wireless communication protocols between the sensor data processing module and the receiver due to its small size and low-power RF radio.

The robot motion information is obtained through the IMU unit. The attitude information (orientation of the robot) is obtained through the integration of the angular rate measurements at a frequency of 100 Hz. The KF-based localization and slip estimation scheme is updated at a frequency of 125 Hz. The wheel encoder reading and the PID motion control algorithm are implemented at a frequency of 4 and 16 Hz, respectively.

B. Simultaneous Robot Localization and Wheel Slip Estimation Scheme

The robot localization and wheel slip estimation are based on the robot kinematics. Fig. 4 shows the kinematic schematic of the skid-steered robot. To obtain a tractable kinematic model, we constrain the robot motion that each side's two wheels rotate at the same speed. We assume that the mass center of the robot is located at the geometric center of the body frame and that the

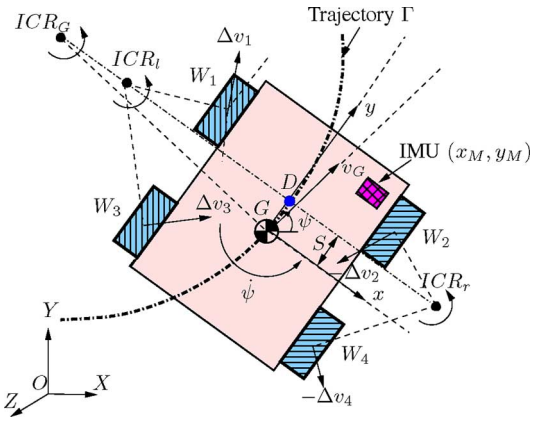

Fig. 4. Kinematic schematic of the skid-steered robot.

robot's four wheels are always in contact with the planar ground surface.

Denote the wheel angular velocities ω_i, $i = 1, \ldots, 4$, for front-left, front-right, rear-left, and rear-right wheels, respectively. From motion constraints, we have

$$\omega_1 = \omega_3 =: \omega_L, \quad \omega_2 = \omega_4 =: \omega_R. \tag{1}$$

Denote the velocities of wheel centers as v_i, $i = 1, \ldots, 4$, for front-left, front-right, rear-left, and rear-right wheels, respectively. The velocity of the robot mass center is denoted by v_G. We define a fixed inertial frame $\mathbf{I}\,(X, Y, Z)$ and a robot body frame $\mathbf{B}\,(x, y, z)$, as shown in Fig. 4. The yaw angle (around the z-axis) is denoted by ψ.

For the IMU located at (x_M, y_M) in the body frame $\mathbf{B}$, we obtain the IMU velocity v_M in $\mathbf{B}$ as

$$v_{Mx} = v_{Gx} - y_M\dot{\psi}, \qquad v_{My} = v_{Gy} + x_M\dot{\psi}. \tag{2}$$

Wheel slip λ_i at the ith wheel is defined as the ratio of the relative velocity of the wheel contact point and the wheel velocity, namely,

$$\lambda_i = \frac{r\omega_i - v_{iy}}{r\omega_i}, \quad i = 1, \ldots, 4 \tag{3}$$

where r is the effective wheel radius. For left- and right-side wheels, the wheel slips satisfy

$$\lambda_1 = \lambda_3 =: \lambda_L, \quad \lambda_2 = \lambda_4 =: \lambda_R$$

due to the robot operating assumption. It is also observed that the wheel slip $\lambda \in (-\infty, 0]$ if the wheel is under braking. To constrain the slip calculation within $\lambda \in [-1, 1]$, using the same treatment in [14], we take $\lambda = -1$ if $\lambda < -1$ during braking.

We denote the instantaneous center of rotation (ICR) of the left-side wheel contact points, right-side wheel contact points, and the robot body as ICR_l, ICR_r, and ICR_G, respectively. It is known that ICR_l, ICR_r, and ICR_G lie on a line parallel to the x-axis [15]. Thus, the y-coordinate S of the ICRs satisfies

$$S = y_l = y_r = y_G = \frac{v_{Gx}}{\dot{\psi}}. \tag{4}$$

Denote the position and velocity vectors of the IMU in the frame $\mathbf{I}$ by $\mathbf{P}_I \in \mathbb{R}^3$ and $\mathbf{V}_I \in \mathbb{R}^3$, respectively. Denote the measured acceleration in the body frame $\mathbf{B}$ by $\mathbf{A}_B \in \mathbb{R}^3$. We obtain the kinematic motion equations, given by

$$\dot{\mathbf{P}}_I = \mathbf{V}_I \tag{5a}$$

$$\dot{\mathbf{V}}_I = C_B^I(\mathbf{A}_B + \mathbf{w}_1) + \mathbf{G} \tag{5b}$$

where $\mathbf{G} = [0 \;\; 0 \;\; -g]^T$, g is the gravitational constant, and $\mathbf{w}_1 = [w_{ax} \; w_{ay} \; w_{az}]^T$ is the IMU measurement noise along the x-, y-, and z-axes, respectively. $C_B^I \in \mathrm{SO}(3)$ is the rotational transformation matrix from frames $\mathbf{B}$ to $\mathbf{I}$ [13].

In order to estimate the location $\mathbf{P}_I$ and wheel slips simultaneously, we consider the robot velocity constraints. First, it is straightforward to obtain the following velocity constraint:

$$v_{Mz} = 0. \tag{6}$$

The longitudinal velocity v_{My} is obtained by incorporating the wheel encoder measurements with wheel slip estimates

$$v_{My} = \frac{r}{2}\left[(\omega_L + \omega_R) - (\lambda'_L\omega_L + \lambda'_R\omega_R)\right] + x_M\dot{\psi} \tag{7}$$

where

$$\lambda'_L(\lambda'_R) = \begin{cases} \max\{\lambda_L(\lambda_R), 0\}, & \text{if } \omega_L \geq \omega_R (\omega_L \leq \omega_R) \\ \min\{\lambda_L(\lambda_R), 0\}, & \text{if } \omega_L < \omega_R (\omega_L > \omega_R). \end{cases}$$

For the lateral velocity v_{Mx}, from (2) and (4), we obtain

$$v_{Mx} = (S - y_M)\dot{\psi}. \tag{8}$$

Here, we estimate the y-axis coordinate S of ICRs by curve-fitting experimental data. With the IMU velocity constraints given by (6)–(8), we designed a KF-based localization and slip estimation scheme [13].

III. Tire Deformation Sensing Models

In this section, we present mathematical sensor models to demonstrate a relationship between the measured electric voltage (charge) and the underlying wheel/ground interaction information. Fig. 5(a) shows the schematic diagram of the PVDF-based deformation sensor attached to the tire inner surface. We assume that the sensor is perfectly attached to the tire inner surface, and the strain is continuous across the sensor/tread layers. The PVDF sensor is initially curved along the tire inner surface. When the tire rotates at the contact patch, the PVDF sensor then deforms flat on the contact patch [Fig. 5(a)]. Due to such a deformation, the PVDF sensor generates electric charge. Moreover, when the tire tread contacts with the ground, the tread is also under compression or tension, which essentially generates the traction/braking forces and self-aligned moment [16]. In the following, we first consider the bending effect, and then the stretching effect, of the rubber tread on sensor outputs.

A. Sensor/Rubber Bending Model

We assume that the tire/ground contact patch is of rectangular shape with a length L and a width B, respectively. For simplicity, we assume that the wheel/ground contact pressure per unit length, denoted by p, is uniformly distributed across the contact patch, i.e., $p = p_0$. We also denote the PVDF sensor size by l (length), b (width), and t_S (thickness), respectively. The length

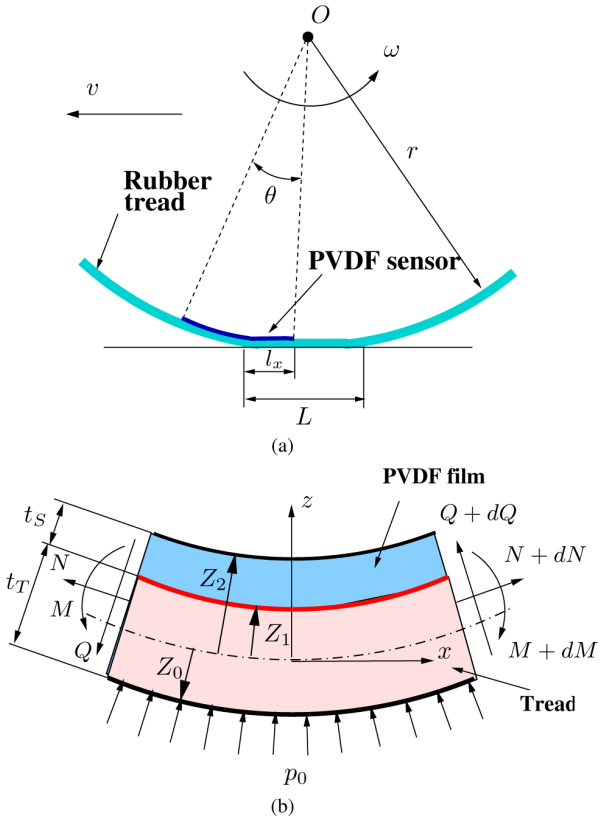

Fig. 5. (a) Schematic of the tire rubber tread and the PVDF deformation sensor. (b) PVDF/tread layers element under deformation.

of the deformed portion of the PVDF sensor is denoted as l_x. The thickness of the tire rubber layer is denoted as t_T. We consider a differential element of the PVDF film with the tire tread under the deformation, as shown in Fig. 5(b).

We denote the coordinate system x–z along the neutral axis and the deflections by $u(x,t)$ and $w(x,t)$ in the x- and z-directions, respectively [Fig. 5(b)]. Considering that the neutral axis of the PVDF/tread layers is located at a distance of Z_1 under the PVDF/tread interface surface, we have $Z_2 = Z_1 + t_S$ and $Z_0 = Z_1 - t_T$. We denote the strain inside the PVDF/tread layers as $\epsilon(x,z)$. By the assumption that the strain is distributed linearly across the PVDF/tread layers, we have

$$\epsilon(x,z) = \epsilon_0(x) + z\kappa(x) \tag{9}$$

where $\epsilon_0(x)$ represents the strain along the neutral axis surface and $\kappa(x)$ represents the bending strain or changes in the curvature of the neutral surface during the deformation [17]. Moreover, we have the following relationships:

$$\epsilon_0(x) = \frac{\partial u}{\partial x} + \frac{w}{r}, \quad \kappa(x) \approx -\frac{\partial^2 w}{\partial x^2}. \tag{10}$$

where r is the tire radius. For the differential element in Fig. 5(b), we can write a force and moment balance, and obtain the equations of motion for the PVDF/tread layers as follows:[1]

$$\begin{bmatrix} L_{11} & L_{13} \\ L_{31} & L_{33} \end{bmatrix} \begin{bmatrix} u \\ w \end{bmatrix} = \begin{bmatrix} \rho & 0 \\ 0 & \rho \end{bmatrix} \frac{\partial^2}{\partial t^2} \begin{bmatrix} u \\ w \end{bmatrix} + \begin{bmatrix} 0 \\ p_0 \end{bmatrix} \tag{11}$$

[1]We omit the derivation in detail and readers can refer to [17].

where ρ is the mass density of the PVDF/tread layers and

$$L_{11} = A_1 \frac{\partial^2}{\partial x^2}, \quad L_{13} = L_{31} = \frac{A_1}{r}\frac{\partial}{\partial x} - A_2 \frac{\partial^3}{\partial x^3}$$

$$L_{33} = \frac{A_1}{r^2} - \frac{2A_2}{r}\frac{\partial^2}{\partial x^2} + A_3 \frac{\partial^4}{\partial x^4}$$

and

$$A_k = \frac{1}{k} b \sum_{i=1}^{2} c_{i11}\left(Z_i^k - Z_{i-1}^k\right), \quad k = 1, 2, 3.$$

In the previous equations, c_{i11}, $i = 1, 2$, is the stiffness matrix component (elastic modulus) of the ith layer along the $x(1)$-direction. A linear relationship between the stress σ_1 and strain ϵ_1 in the $x(1)$-direction, $\sigma_1 = c_{i11}\epsilon_1$, is used for the ith layer.

Notice that, since the tire tread thickness t_T (in millimeters scale) is much larger than the PVDF film thickness t_S (in micrometers scale), the neutral axis can thus be approximated at the center of the tire tread cross section, and we obtain

$$Z_1 = -Z_0 = \frac{1}{2}t_T, \quad Z_2 - Z_1 = t_S, \quad \text{and} \quad Z_2 = \frac{1}{2}t_T$$

and

$$A_1 = b(c_{111}t_T + c_{211}t_S), \quad A_2 = \frac{1}{2}bc_{211}t_S t_T$$

$$A_3 = \frac{1}{12}b(c_{111}t_T + 3c_{211}t_S)t_T^2. \tag{12}$$

Assuming the zero strain at the neutral axis, i.e., $\epsilon_0(x) = 0$, and applying the boundary conditions

$$w(0) = w(l_x) = 0, \quad M(0) = M(l_x) = 0 \tag{13}$$

we obtain a quasi-static solution $w(x)$ for equations of motion given by (11) as

$$w(x) = \frac{p_0 r}{A_2}\left[\frac{1}{\alpha^2}\cosh(\alpha x) - \frac{1}{\alpha^2}\frac{\cosh(\alpha l_x) - 1}{\sinh(\alpha l_x)}\sinh(\alpha x) - \frac{1}{\alpha^2} + \frac{l_x}{2}x - \frac{1}{2}x^2\right] \tag{14}$$

where $\alpha = \sqrt{A_2/rA_3}$.

We consider the linear constitutive relationship for PVDF piezoelectricity among strain (stress) and electric field (electric displacement) [18]. Moreover, we assume that the electric field is approximately close to zero due to the quasi-static estimation in this study. The accumulated electric charge due to bending is calculated as

$$q_b = \int_A D_3 dA = d_{31}c_{211}\int_A \epsilon_1\, dA.$$

Using (10), we write the previous equation explicitly by integrating on the electrodes surface area A as

$$q_b(l_x) = -bd_{31}c_{211}t_T\int_0^{l_x}\frac{\partial^2 w}{\partial x^2}dx = \frac{2d_{31}p_0 r}{t_S}\left[l_x - \frac{2}{\alpha}\frac{e^{\alpha l_x} - 1}{e^{\alpha l_x} + 1}\right] \tag{15}$$

where we use (12) and (14) in the last step.

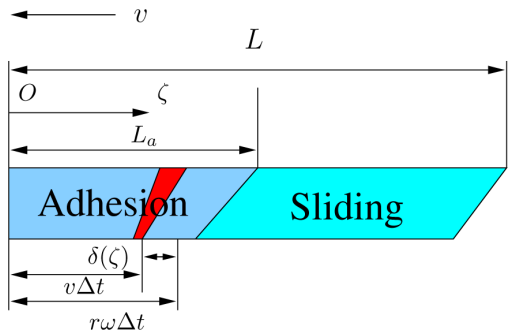

Fig. 6. Tire/road physical model schematic of the wheel/ground contact deformation during traction.

From (15), we observe that the generated charge $q_b(l_x)$ is a function of the sensor contact length l_x, $q(0) = 0$, and

$$q_b'(l_x) := \frac{dq(l_x)}{dl_x} = \frac{2d_{31}p_0 r}{t_S}\left(\frac{e^{\alpha l_x}-1}{e^{\alpha l_x}+1}\right)^2 \geq 0. \tag{16}$$

The above calculation implies that the maximum charge q_{bm} due to bending is achieved at the location where the whole sensor film deforms completely flat, namely, $l_x = l$. Such an observation will be used in our later discussion.

B. Sensor/Rubber Stretching Model

The wheel rubber tread is stretched (or compressed) throughout the contact patch surface to produce traction/braking forces (moments). Since the sensor is attached on the wheel's inner rubber surface, the sensor film is also stretched (compressed). The sensor output should reflect such a stretching effect.

Here, we take a pseudostatic physical model to capture the wheel/ground friction properties [16]. The basic idea of the physical model is to divide the wheel/ground contact patch into an adhesion region and a sliding region. In the adhesion region, the interacting forces depend on the elastic properties of the tire, whereas in the sliding region, the interacting forces depend on the adhesive properties of the tire/road interface [19]. Fig. 6 shows a rectangular shaped contact patch under such a division for a traction case.

A moving coordinate system $O\zeta$ is set up as shown in Fig. 6 with the origin O at the front extremity of the contact patch length and at the center of the contact patch width. We assume that there is a critical length $L_a \leq L$ such that for the adhesion region, $0 \leq \zeta < L_a$, and for the sliding region, $L_a \leq \zeta \leq L$. Instead of considering a uniform distribution, we assume a more realistic wheel/ground contact pressure distribution per unit length as

$$p(\zeta) = \frac{4P_{\rm m}}{L}\zeta\left(1-\frac{\zeta}{L}\right)$$

where $P_{\rm m} = 1.5F_z/BL$ and F_z is the normal load at each wheel [19].

We consider that the wheel is under a traction motion, as shown in Fig. 6. For the adhesion region $0 \leq \zeta < L_a$, we can calculate the deformation $\delta(\zeta)$ within a time period Δt as

$$\delta(\zeta) = r\omega\,\Delta t - v\,\Delta t, \quad \text{and} \quad \zeta = r\omega\,\Delta t.$$

Therefore, we obtain

$$\delta(\zeta) = \frac{r\omega - v}{r\omega}\zeta = \lambda\zeta. \tag{17}$$

The strain of the rubber at ζ is $\epsilon_a(\zeta) = \delta(\zeta)/L = \lambda\xi$, where $\xi := \zeta/L$ is the normalized coordinate along the contact patch length direction. Let the wheel's longitudinal stiffness rate per unit area be k_x, and we can obtain the friction force for a small slip value $\lambda \ll 1$ (in this case, $L_a \approx L$, and the whole contact patch is an adhesion region) as

$$F_{xa} = \int_0^L k_x\delta(\zeta)B\,d\zeta = \frac{1}{2}k_x BL^2\lambda. \tag{18}$$

We consider that the wheel's longitudinal stiffness C_x is the slope of the F_x–λ curve, namely,

$$C_x = \left.\frac{dF_x}{d\lambda}\right|_{\lambda=0}$$

and from (18), we have

$$k_x = \frac{2C_x}{BL^2}. \tag{19}$$

The previous equation can be used to calculate k_x for a given C_x, which is typically obtained experimentally.

For the sliding region, we denote the sliding friction coefficient between the wheel and the ground as μ_x. The stress distribution can be obtained in a similar fashion as $\sigma_s(\zeta) = \mu_x p(\zeta)$, and the strain distribution is then $\epsilon_s(\zeta) = \mu_x p(\zeta)/k_x L$.

From the previous calculation, we obtain the stress distribution $\sigma(\zeta)$ on the contact patch

$$\sigma(\zeta) = \begin{cases} k_x\lambda\zeta, & 0 \leq \zeta < L_a \\ \dfrac{4P_{\rm m}\mu_x}{L}\zeta\left(1-\dfrac{\zeta}{L}\right), & L_a \leq \zeta \leq L \end{cases} \tag{20}$$

and the strain distribution $\epsilon(\xi)$

$$\epsilon(\xi) = \begin{cases} \lambda\xi, & 0 \leq \xi < \xi_a \\ \dfrac{4P_{\rm m}\mu_x}{k_x L}\xi\,(1-\xi), & \xi_a \leq \xi \leq 1 \end{cases} \tag{21}$$

where $\xi_a := L_a/L$.

For a continuous stress distribution at $\zeta = L_a$, from (20), we have

$$L_a = (1 - C_x/3\mu_x F_z\lambda)\,L \tag{22}$$

and a condition of $\lambda \leq \lambda_{\rm cr} := 3\mu_x F_z/C_x$ can be found for a critical slip $\lambda_{\rm cr} \leq 1$. Fig. 7 shows a schematic of strain distribution along the contact patch length direction during traction. Note that the sensor is assumed to be perfectly attached to the rubber surface, and thus, it is appropriately assumed that the strain at the glued side of the sensor surface is the same as that on the inner rubber surface given by (21).

We are now ready to calculate the sensor model due to rubber tread stretching. We consider the case when the sensor length is shorter than the contact patch length, namely, $l \leq L$. We also

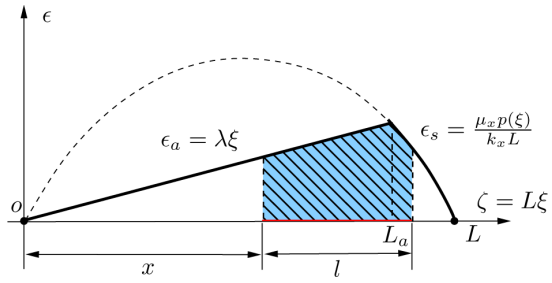

Fig. 7. Stress distribution along the contact patch length during traction.

assume that the wheel slip satisfies $\lambda \leq \lambda_{\rm cr}$ since the robot is in a stable run.[2] For such a small slip range, we assume that $L - L_a \leq l \leq L_a$. Fig. 7 shows the sensor film strain distribution $\epsilon(\zeta)$ when the location of the leaving edge of the sensor film is at $\zeta = x$. At such a location, we obtain the electric charge due to contact patch stretching as

$$q_s(x) = \int_x^{x+l} d_{31}\sigma(\zeta) b\, d\zeta = d_{31} b c_{11} \int_x^{x+l} \epsilon(\zeta) d\zeta$$

where c_{11} is the elastic modulus of the PVDF film along the $x(1)$-direction. Note that the previous integration is indeed the shaded area shown in Fig. 7. We consider a location x at which $q_s(x)$ achieves its maximum value only for $L_a - l \leq x \leq L_a$, because otherwise, $q_s(x)$ can always be increased by choosing an $x \in [L_a - l,\ L_a]$. Thus, we obtain

$$\begin{aligned} q_s(x) &= d_{31} b c_{11} \left[\int_x^{L_a} \frac{\lambda}{L} \zeta d\zeta + \int_{L_a}^{x+l} \frac{4P_{\rm m}\mu_x}{k_x L^2} \zeta \left(1 - \frac{\zeta}{L}\right) d\zeta \right] \\ &= \frac{d_{31} c_{11} b}{6L} \left\{ 3\left(L_a^2 - x^2\right) + \frac{3L}{L - L_a}\left[(x+l)^2 - L_a^2\right] \right. \\ &\qquad \left. - \frac{2}{L - L_a}\left[(x+l)^3 - L_a^3\right] \right\} \lambda \end{aligned} \tag{23}$$

where, in the last step, we use the fact $4P_{\rm m}\mu_x/(k_x L^2) = \lambda/(L - L_a)$ from (22). To calculate the location $\zeta = x_m$ at which $q_s(x)$ achieves its maximum value, we take the derivative of $q_s(x)$ in (23), and thus, obtain

$$\begin{aligned} \frac{dq_s}{dx} &= -\frac{d_{31} c_{11} b\lambda}{L(L - L_a)}\left[x^2 + (2l - L_a)x + l(l - L)\right] \\ &= -\frac{d_{31} c_{11} b\lambda}{L(L - L_a)} f(x) \end{aligned} \tag{24}$$

where $f(x) = x^2 + (2l - L_a)x + l(l - L)$, and

$$\frac{d^2 q_s}{dx^2} = -\frac{d_{31} c_{11} b\lambda}{L(L - L_a)}\left[2(x + l) - L_a\right] < 0$$

for $x \in [L_a - l,\ L_a]$. Note that function $f(x)$ satisfies $f(L_a - l) = -l(L - L_a) < 0$ and $f(L_a) = l(l + 2L_a - L) > 0$, and thus, there exists an $x_m \in [L_a - l,\ L_a]$ such that $q_s(x)$ achieves its maximum value at x_m. Letting $dq_s/dx|_{x=x_m} = 0$ in (24), we obtain

$$x_m = \frac{-(2l - L_a) + \sqrt{L_a^2 + 4l(L - L_a)}}{2}.$$

Since λ is small, we can approximate x_m by taking $L_a \approx L$ and obtain $x_m \approx L_a - l$. The maximum charge is then

$$q_{\rm sm} = \frac{1}{2L} d_{31} c_{11} b l (2L_a - l)\lambda = K\lambda \tag{25}$$

where

$$K = \frac{d_{31} c_{11} b l (2L_a - l)}{2L}. \tag{26}$$

[2]When the wheel slip is large, such as $\lambda > \lambda_{\rm cr}$, the wheel begins a significant sliding motion and becomes unstable when the wheel is completely sliding on the ground [16].

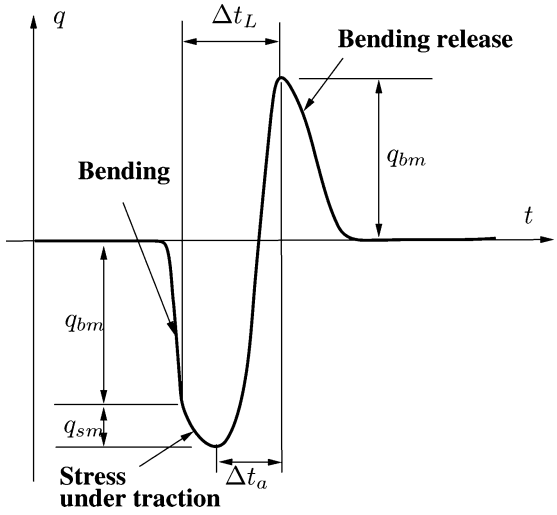

Fig. 8. Schematic of the charge measurement.

C. Combined Sensor Models

With both bending and stretching models, we summarize the expected sensor measurement output.

Fig. 8 shows the schematic of the generated charge of the PVDF sensor going through the wheel/ground contact patch. In the figure, we clearly see the output charge generated by the sensor in three stages: first, the bending motion produces a maximum charge of $q_{\rm bm}$, as given in (15) when the sensor reaches the contact patch completely, namely, $l_x = l$. Second, the traction/braking action on the contact patch generates an extra charge with a maximum value of $q_{\rm sm}$ given in (25). Finally, when the sensor is leaving the contact patch, it creates a charge that is the same magnitude of q_b but in the opposite direction due to the release of the sensor film into its initial precurved state. The sign of the generated charge depends on the poling direction of the PVDF film and the orientation of the sensor attached to the inner tire surface.

Note that in Fig. 8, $\Delta t_L = L/r\omega$ represents the sensor traveling time (at wheel velocity $r\omega$) from the location where the sensor is just completely compressed flat on the contact patch to the location where it is just completely released; $\Delta t_a = (l + L - L_a)/r\omega$ represents the sensor traveling time (at wheel velocity $r\omega$) from the location where q_s achieves its maximum value to the location where it is just completely

Fig. 9. Computer-vision-based localization system. A high-resolution camera is located at a high location to localize and record the position information of a skid-steered mobile robot.

released. Due to the dynamic motion of the tire and grooves on the rubber tread, the generated charge q_b under rubber bending could vary from one cycle to another cycle (we will see such a variation in the next section). Fortunately, we can use the measured q_{sm} (by taking the difference between the positive and negative maximum peak magnitude values in charge measurements) and time difference Δt_a to calculate the contact patch friction characteristics. We next show experimental results.

IV. Experiments

For the integrated tire deformation sensing system shown in Fig. 1, we use a stand-alone computer vision-based positioning system (shown in Fig. 9) as a benchmark to compare and validate the robot localization and wheel slip estimation results. Two PVDF sensors are located inside the front-right wheel, and the sensor outputs are converted and amplified to a range of 0–3.3 V, namely, the output of the sensor without any deformation is around 1.65 V. The amplifier sensitivity is around 0.5 mV/pC. A 10 bit A/D conversion is used to sample sensor measurements, and the sampled data are then wireless transmitted at a frequency of 400 Hz.

We first show the nonlinear KF-based slip estimation results. Fig. 10(a) and (b) shows the slip estimates of the robot on the concrete and sand ground conditions, respectively, with the same wheel velocity combination $\omega_L/\omega_R = 120/60$ rpm. We plot the computer-vision-based slip information in each case for comparison purposes. We choose these two ground conditions because such two cases represent different slip values. For example, we observe positive and large slip values of both sides' wheels on the sand surface, while on the concrete surface, the right side's wheel slip is negative and close to zero [as shown in Fig. 10(a)]. The comparisons with the computer-vision-based results clearly show the estimation scheme captures the slip values in real time.

Fig. 11 shows the deformation measurements from two PVDF sensors that are mounted at a distance of 30 mm along the wheel movement direction. The robot runs at left/right sides' wheel speed 60/80 rpm. From Fig. 11(a), we notice that the maximum magnitudes of sensor measurements of both sensors vary from one cycle to another cycle. Such a variation could be due to

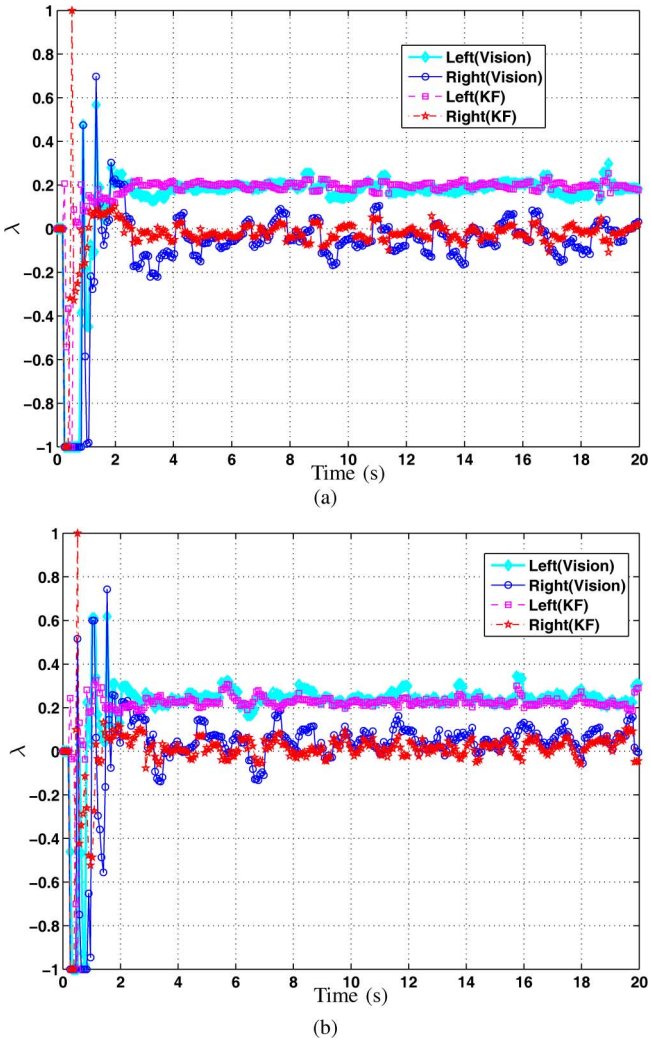

Fig. 10. Estimated wheel slip values using KF-based and computer-vision-based localization schemes with a wheel speed combination $\omega_L/\omega_R = 120/60$ rpm under two ground conditions. (a) Concrete surface. (b) Sand surface.

dynamic robot and wheel running conditions and sensor noises. Comparing with the sensor output schematic in Fig. 8, the actual sensor measurements in Fig. 11(b) show a similar pattern except an extra precontact and a postcontact "bump." Those opposite-direction bumps are due to the fact that, right before the sensor film reaches the contact patch, it already deforms in the opposite direction because of the compliance and continuity of the rubber wheel. We also observe a different shape for the two sensors due to the difference between signal amplification sensitivities for these sensors and sensor mounting variations.

Because of the cycle-to-cycle variation shown in Fig. 11(a), we consider the use of the contact patch-stretching-induced charge $q_{\rm sm}$, rather than the rubber-bending-induced charge $q_{\rm bm}$, to validate our analysis. The reason for such a choice is that $q_{\rm sm}$ can be calculated by the difference of the maximum and the minimum peak magnitude values within each cycle. Although there are variations among measurement cycles, such a differential value of $q_{\rm sm}$ can eliminate or reduce systematic cycle-to-cycle variations and measurement noises.

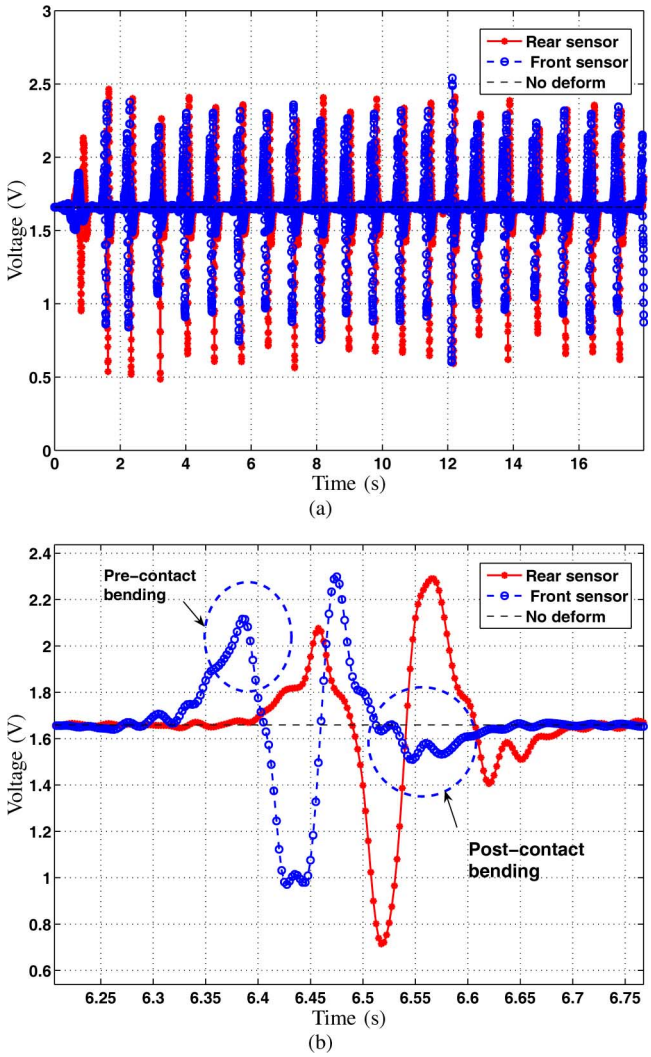

Fig. 11. Sensing data from two PVDF sensors located one wheel with a separate distance of 30 mm. The robot is running at a wheel velocity combination of $\omega_L/\omega_R = 60/80$ rpm. (a) 18 s sensor measurements. (b) Detailed one-cycle sensor measurement.

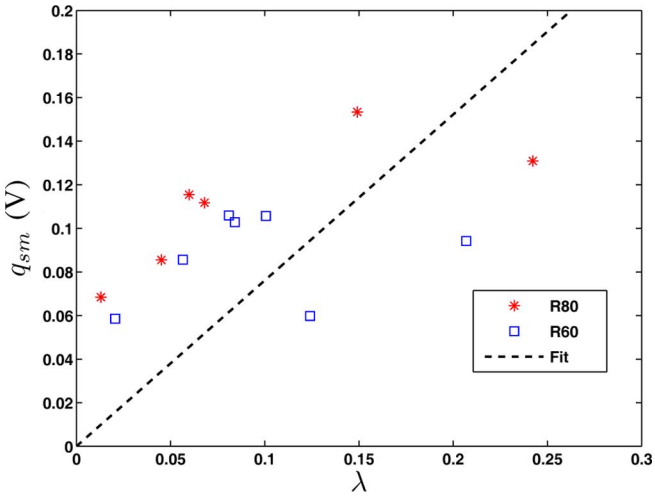

Fig. 12. Measured maximum charge due to wheel contact patch stretch under different wheel velocities.

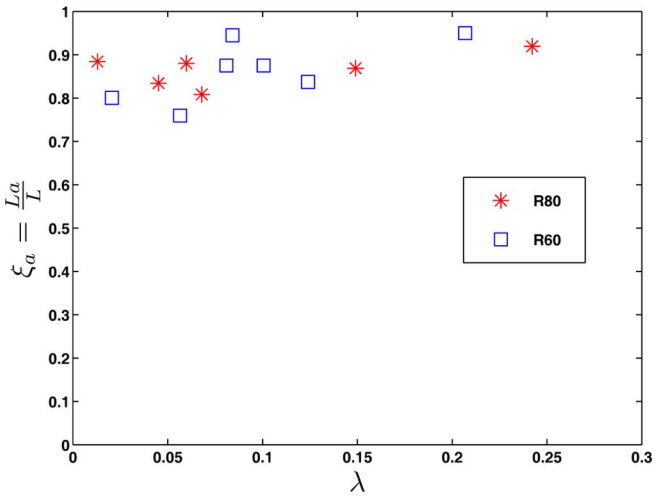

Fig. 13. Normalized adhesion length $\xi_a = L_a/L$ versus slip values under different wheel velocities.

TABLE I
ROBOTIC SYSTEM PARAMETERS AND ESTIMATION RESULTS

l (mm)	b (mm)	Mass (kg)	B (mm)	L (mm)	r (mm)	C_x (N)	μ_x
20	3	10.9	89	46	87	52.7	0.47

We run the robot under a set of wheel velocity combinations on the same concrete ground surface. The wheel with the embedded sensors inside is commanded at a fixed velocity of 60 or 80 rpm. We then change the other side's wheel velocities from 20 to 140 rpm with an increase of 20 rpm in each run. By doing so, we can generate a range of slip values at the sensed wheel.

Fig. 12 shows the measured charge $q_{\rm sm}$ (in voltage) versus the estimated wheel slip values under $\omega_R = 60$ and 80 rpm. The measurements in Fig. 12 demonstrate a roughly linear relationship, as shown in the analysis given by (25). In principle, we can use the estimate of the slope value K in Fig. 12 to calculate the parameter L_a by (26). However, our calculation shows a large error due to the lack of accurate measurement of the amplifier sensitivity (from electric charge to voltage).

Therefore, instead of using the slope value K to estimate L_a, we consider utilizing time difference Δt_a (illustrated in Fig. 8) between the maximum and the minimum peaks within each cycle. Note that $L_a = L + l - r\omega\,\Delta t_a$ by the analysis, and we can estimate L_a for a known Δt_a. Fig. 13 shows an estimate of normalized length $\xi_a = L_a/L$ of the adhesion region over the contact patch lengths versus slip values. We measure the contact patch length L, as listed in Table I.

From Fig. 13, we find that the normalized adhesion region length ξ_a is almost constant under various slip values. However, from (22), a linear relationship (with a small negative slope) should be expected. We consider that such a discrepancy is probably due to the variations of the measurements and the low-frequency sampling rate for the sensor signals. We also use the acceleration data to estimate the tire stiffness C_x as shown in Table I. Using the estimate of L_a and (22), we calculate the wheel/ground sliding friction coefficients μ_x under both wheel velocities $\omega_R = 60$ and 80 rpm. Both μ_x estimates are

close to each other, around 0.47 as listed in Table I since the robot is running on the same ground surface. Therefore, the experiments have demonstrated that the sensor measurements can provide underlying friction characteristics of wheel/ground interactions.

V. Conclusion and Future Work

We presented a prototype of a wheel tread deformation sensing system for "smart tire" applications for mobile robots and vehicles. A PVDF-based sensor was used and embedded inside a wheel to measure the rubber tread deformation. We presented an analytical sensing output model that can be used to capture the wheel/ground friction characteristics. A skid-steered robotic platform was developed as a testbed to demonstrate and validate the sensor models and measurements. The preliminary testing data has shown the feasibility of the estimate of wheel/ground interactions, such as wheel slip and friction coefficient. We are currently working on the optimization of the sensor size and the embedded location, and using multiple embedded sensor arrays to enhance the sensor measurements. We are also likely to further incorporate the sensor measurements into newly developed wheel/ground dynamic friction models, such as those in [20]–[23], for a sensor-enabled estimation and control scheme. We will report new developments in the future.

Acknowledgment

The author thanks J. Zhang, B. Mika, C.-Y. Kim, and B. Greens for their help of experiment developments. He is also grateful to Prof. D. Song, Prof. H. Liang, Prof. S. Jayasuriya, and Prof. R. Langari at Texas A&M University and Dr. E. H. Tseng and Dr. D. Hrovat at Ford Research Laboratories for their help and discussions.

References

[1] S. Gruber, M. Semsch, T. Strothjohann, and B. Breuer, "Elements of a mechatronic vehicle corner," *Mechatronics*, vol. 12, no. 8, pp. 1069–1080, 2002.

[2] S. Müller, M. Uchanski, and K. Hedrick, "Estimation of the maximum tire–road friction coefficient," *ASME J. Dyn. Syst., Meas., Control*, vol. 125, no. 4, pp. 607–617, 2003.

[3] APOLLO Consortium, "Intelligent Tyre Systems—State of the Art and Potential Technologies," Technical Research Centre of Finland (VTT), APOLLO Deliverable D7 for Project IST-2001-34372, 2003.

[4] O. Yilmazoglu, M. Brandt, J. Sigmund, E. Genc, and H. Hartnagel, "Integrated InAs/GaSb 3D magnetic field sensors for the intelligent tire," *Sens. Actuators A*, vol. 94, pp. 59–63, 2001.

[5] A. Pohl, R. Steindl, and L. Reindl, "The intelligent tire utilizing passive SAW sensors—Measurement of tire friction," *IEEE Trans. Instrum. Meas.*, vol. 48, no. 6, pp. 1041–1046, Dec. 1999.

[6] R. Matsuzaki and A. Todoroki, "Passive wireless strain monitoring of actual tire using capacitance–resistance change and multiple spectral features," *Sens. Actuators A*, vol. 126, pp. 277–286, 2006.

[7] R. Matsuzaki and A. Todoroki, "Wireless flexible capacitive sensor based on ultra-flexible epoxy resin for strain measurement of automobile tires," *Sens. Actuators A*, vol. 140, pp. 32–42, 2007.

[8] F. Braghin, M. Brusarosco, F. Cheli, A. Cigada, S. Manzoni, and F. Mancosu, "Measurement of contact forces and patch features by means of accelerometers fixed inside the tire to improve future car active control," *Veh. Syst. Dyn.*, vol. 44, Suppl., pp. 3–13, 2006.

[9] M. Palmer, C. C. Boyd, J. McManus, and S. Meller, "Wireless smart-tires for road friction measurement and self state determination," in *Proc. 43rd AIAA/ASME/ASCE/AHS Struct., Struct. Dyn., Mater. Conf.*, Denver, CO, 2002, Paper AIAA-2002-1548.

[10] K. Moon, H. Liang, J. Yi, and B. Mika, "Tire tread deformation sensor and energy harvester development for "smart tire" applications," in *Proc. SPIE*, vol. 6529, 2007, Paper 62590K.

[11] G. Anousaki and K. Kyriakopoulos, "A dead-reckoning scheme for skid-steered vehicles in outdoor environments," in *Proc. IEEE Int. Conf. Robot. Autom.*, New Orleans, LA, 2004, pp. 580–585.

[12] J. Yi, D. Song, J. Zhang, and Z. Goodwin, "Adaptive trajectory tracking control of skid-steered mobile robots," in *Proc. IEEE Int. Conf. Robot. Autom.*, Rome, Italy, 2007, pp. 2605–2610.

[13] J. Yi, J. Zhang, D. Song, and S. Jayasuriya, "IMU-based localization and slip estimation for skid-steered mobile robots," in *Proc. IEEE/RSJ Int. Conf. Intell. Robot. Syst.*, San Diego, CA, 2007, pp. 2845–2850.

[14] M. Kitano and M. Kuma, "An analysis of horizontal plane motion of tracked vehicles," *J. Terramech.*, vol. 14, no. 4, pp. 211–225, 1977.

[15] J. Wong and C. Chiang, "A general theory for skid steering of tracked vehicles on firm ground," *Proc. Inst. Mech. Eng. D: J. Automob. Eng.*, vol. 215, pp. 343–355, 2001.

[16] J. Yi, "A fault tolerant longitudinal control and tire/road friction estimation system for automated highway systems (AHS)," Ph.D. dissertation, Dept. Mech. Eng., Univ. California, Berkeley, 2002.

[17] H. Yoon, G. Washington, and A. Danak, "Modeling, optimization, and design of efficient initially curved piezoceramic unimorphs for energy harvesting applications," *J. Intell. Mater. Sys. Struct.*, vol. 16, no. 10, pp. 877–888, 2005.

[18] *IEEE Standard on Piezoelectricity*. ANSI/IEEE Standard 176-1987, 1987.

[19] G. Gim and P. Nikravesh, "An analytical model of pneumatic tyres for vehicle dynamic simulations. Part I: Pure slips," *Int. J. Veh. Des.*, vol. 11, no. 6, pp. 589–618, 1990.

[20] J. Yi, L. Alvarez, and R. Horowitz, "Adaptive emergency brake control with underestimation of friction coefficient," *IEEE Trans. Control Syst. Technol.*, vol. 10, no. 3, pp. 381–392, May 2002.

[21] J. Yi, L. Alvarez, X. Claeys, and R. Horowitz, "Tire/road friction estimation and emergency braking control using a dynamic friction model," *Veh. Syst. Dyn.*, vol. 39, no. 2, pp. 81–97, 2003.

[22] L. Alvarez, J. Yi, L. Olmos, and R. Horowitz, "Adaptive emergency braking control with observer-based dynamic tire/road friction model and underestimation of friction coefficient," *ASME J. Dyn. Syst., Meas., Control*, vol. 127, no. 1, pp. 22–32, 2005.

[23] J. Deur, J. Asgari, and D. Hrovat, "A 3D brush-type dynamic tire friction model," *Veh. Syst. Dyn.*, vol. 42, no. 3, pp. 133–173, 2004.

Jingang Yi (S'99–M'02–SM'07) received the B.S. degree in electrical engineering from Zhejiang University, Hangzhou, China, in 1993, the M.Eng. degree in precision instruments from Tsinghua University, Beijing, China, in 1996, and the M.A. degree in mathematics and the Ph.D. degree in mechanical engineering from the University of California, Berkeley, in 2001 and 2002, respectively.

From May 2002 to January 2005, he was a member of the Technical Staff, Lam Research Corporation, Fremont, CA. From January 2005 to December 2006, he was with the Department of Mechanical Engineering, Texas A&M University, as a Visiting Assistant Professor. He is currently an Assistant Professor in Mechanical Engineering at San Diego State University, San Diego, CA. His current research interests include autonomous and robotic systems, dynamic systems and control, intelligent sensing and actuation systems, mechatronics, and automation science and engineering, with applications to semiconductor manufacturing and intelligent transportation systems.

Dr. Yi is a member of the American Society of Mechanical Engineers (ASME). He was the recipient of the Kayamori Best Paper Award of the 2005 IEEE International Conference on Robotics and Automation (ICRA) and the Best Conference Paper Finalist of the 2007 IEEE International Conference on Automation Science and Engineering (CASE).